Supporting information for

Boosting interfacial bonding between FeOOH catalysts and Fe₂O₃ photoanodes toward efficient water oxidation

Chenchen Feng[a,c+], Yushui Bi[b,+], Faqi Zhan[c], Yingpu Bi*[a]

[a] State Key Laboratory for Oxo Synthesis & Selective Oxidation, National Engineering Research Center for Fine Petrochemical Intermediates, Lanzhou Institute of Chemical Physics, CAS, Lanzhou 730000, Gansu, China.

[b] School of Chemistry and Pharmaceutical Engineering, Shandong First Medical University & Shandong Academy of Medical Sciences, Taian, Shandong 271016, China.

[c] School of Materials Science and Engineering, State Key Laboratory of Advanced Processing and Recycling of Non-ferrous Metals, Lanzhou University of Technology, 287 Langongping Road, Lanzhou 730050, Gansu, China.

[+] These authors contributed equally to this work.

Corresponding authors: Yingpu Bi, E-mail: yingpubi@licp.cas.cn

Experiment section

1. Preparation of Fe$_2$O$_3$ photoanodes

Firstly, Ti foils (1 cm×5 cm) were cleaned by sonication in acetone, ethanol and deionized water to remove surface impurities, and then treated in hot hydrochloric acid. For the HCl treatment of Ti foils, a cleaned Ti foils were immersed into 30 mL concentrated hydrochloric acid and kept it at 80 °C for 30 min. After that, Ti foils were immediately removed from the hot HCl solution and washed with water for several times. For the hydrothermal growth of FeOOH nanorods, 1.215 g FeCl$_3$·6H$_2$O and 0.27 g urea were dissolved in 60 mL deionized water under vigorous stirring for 30 min. Then the solution was transfer to a Teflon-lined stainless-steel autoclave (80 mL) in which a piece of acid-treated Ti foil was immersed into the solution. Then the autoclave was sealed and maintained at 100 °C for 10 h in an electric oven. After the autoclave cooled down at room temperature naturally, the Ti foil covered with FeOOH nanorods was taken out and washed with water and ethanol for several times, followed by drying at 60 °C. Finally, the precursor film was annealed at 550 °C in air for 2 h to obtain 3D dendritic Fe$_2$O$_3$ photoanode (denoted as Fe$_2$O$_3$). In addition, 1D Fe$_2$O$_3$ nanorod arrays were synthesized by a similar method to that of Fe$_2$O$_3$ by using untreated Ti foil as substrate.

2. Ar plasma surface treatment of Fe$_2$O$_3$ photoanodes

A plasma system (PDC-36G, Hefei Kejing Materials Technology Co., Ltd) was used to modify the surface of Fe$_2$O$_3$ photoanodes at room temperature. The samples (1 cm×2.5 cm) were placed on the quartz boat in a plasma reactor. At last, when the chamber pressure was kept at 40 Pa, the samples were treated using Ar plasma with power of 16 W and the treatment time is 30 min. The treated samples were denoted as Fe$_2$O$_3$(V$_O$).

3. Loading of FeOOH cocatalyst on Fe$_2$O$_3$ photoanodes

For the deposition of FeOOH cocatalyst, the as-prepared photoanodes were immersed in the mixed precursor solution (contains 45 mM urea and 30 mM FeSO$_4$) and kept in the oven at 100 °C for 5 min. After the deposition, the coated photoanodes were rinsed with deionized water, dried in N$_2$ flow. The obtained samples were denoted as Fe$_2$O$_3$(V$_O$)-FeOOH.

4. Characterization

The X-ray diffraction spectra (XRD) measurements were performed on a Rigaku RINT-2000 instrument utilizing Cu Kα radiation (40 KV). The XRD patterns were recorded from 10° to 90°

with a scanning rate of 0.067°/s. Scanning electron microscopy (SEM) measurements were carried out on a field-emission scanning electron microscope (JSM-6701F. JEOL) operated at an accelerating voltage of 5 KV. Transmission electron microscopy (TEM) measurements were carried out by using a FEI Tecnai TF20 microscope operated at 200 kV. UV-vis diffuse reflectance spectra were taken on an UV-2550 (Shimadzu) spectrometer by using $BaSO_4$ as the reference. The element composition was detected by X-ray photoelectron spectroscope (XPS, ESCALAB 250Xi). Photoluminescence spectra and time-resolved photoluminescence spectra were monitored by LP 980 laser flash photolysis instrument (Edinburgh, U.K.). The oxygen vacancies were resolved by electron paramagnetic resonance (EPR) spectrometry (Bruker, EMX PLUS, Germany).

5. Photoelectrochemical measurements

The Photoelectrochemical properties were measured by an electrochemical analyzer (CHI660D) in a standard three-electrode system with the as-prepared photoanode serving as the working electrode, a Pt foil as the counter electrode, and a saturated Ag/AgCl (saturated KCl) as a reference electrode. The illumination source was a 300 W Xe arc lamp (Beijing Perfectlight Technology Co. Ltd., Microsolar 300 UV) equipped with an AM 1.5G filter, and the power intensity of the incident light was calibrated to 100 mW/cm^2 at the surface of the working electrode. The irradiation area was controlled at 1 cm^2. The current-voltage (*J-V*) characteristic of the electrodes, with a scan rate of 10 mV/s. A 1 M KOH aqueous solution (pH 13.6) was used as the electrolyte. All potentials of the working electrode were presented against the reversible hydrogen electrode (RHE).

$$E_{RHE} = E_{Ag/AgCl} + E_{Ag/AgCl}\ (reference) + 0.0591 \times pH$$

($E_{Ag/AgCl}$ (reference) = 0.1976 V vs. NHE at 25°C)

Where pH is a pH value of the electrolyte.

The IPCE was determined using a motorized monochromator (Oriel Cornerstone 130 1/8 m). IPCE was measured at 1.23 V vs. RHE in 0.1 M KOH aqueous solution (pH 13.6) using the same three-electrode setup described above for photocurrent measurements. IPCE was calculated as follows:

$$IPCE = \frac{1240 \times I(mA/cm^2)}{P_{light}(mW/cm^2) \times \lambda(nm)} \times 100\%$$

Where *I* is the measured photocurrent density at a specific wavelength, λ is the wavelength of

incident light and P_{light} is the measured light power density at that wavelength.

The ABPE was calculated by following equation:

$$ABPE(\%) = \frac{I(mA/cm^2) \times (1.23 - V_{bias})(V)}{P_{light}(mW/cm^2)} \times 100\%$$

Where I is the photocurrent density from the I-V curve shown in Figure 3A, V_{bias} (vs. RHE) is the applied bias, P_{light} is the incident illumination power density (100 mW cm^{-2}).

The electrochemical impedance spectroscopy (EIS) Nyquist plots were measured in a 1.0 M KOH aqueous solution at 1.23 V (vs. RHE) with small AC amplitude of 10 mV in the frequency range of 0.1 to 10^5 Hz under AM 1.5G illumination (100 mW/cm^2). The measured spectra were fitted with Z-view software.

Light absorptance of a semiconductor can be calculated using the following equation:

$$\eta_{light} = 1 - 10^{-A}$$

$$A = 1 - Reflectance - Transmittance$$

Reflectance (R) and Transmittance (T) were measured experimentally by UV-vis spectroscopy.

The photocurrent density arising from PEC performance (PEC) can be described as following:

$$J_{PEC} = J_{abs} \times \eta_{separation} \times \eta_{injection}$$

where J_{abs} is the photocurrent density when completely converting the absorbed photons into current (i.e., absorbed photon-to-current efficiency (APCE) = 100 %). Adding 0.5 M H_2O_2 into the electrolyte (1 M KOH) can largely suppress the surface recombination of charge carriers without influencing the charge separation in the electrode bulk (i.e., $\eta_{injection}$ could be regarded as 100 %). Therefore, $\eta_{separation}$ and $\eta_{injection}$ can be determined as following:

$$\eta_{separation} = J_{H_2O_2}/J_{abs}$$

$$\eta_{injection} = J_{H_2O}/J_{H_2O_2}$$

Where J_{H_2O} and $J_{H_2O_2}$ is the photocurrent density for PEC H_2O oxidation and H_2O_2 oxidation, respectively.

6. Detection of the amount of hydrogen and oxygen evolution

To quantitatively determine the amount of H_2 and O_2 produced from the overall water splitting, an online gas analysis system (Labsolar 6A, Beijing Perfectlight Technology Co. Ltd.) and a gas chromatograph (GC 7890A, Agilent Technologies) were employed. The produce of H_2 and O_2 was

performed in a three-electrode system at a constant bias of 1.23 V vs. RHE under AM 1.5G illumination (100 mW cm^{-2}).

The Faradaic efficiency was calculated by dividing the amount of gas detected by the theoretical amount of gas calculated on the basis of the total charge passed, using the following equation:

$$FE(\%) = \frac{A \times n(mol) \times F(C\ mol^{-1})}{Charge\ passed\ through\ WE\ (C)} \times 100$$

where n is moles of evolved H$_2$ or O$_2$ gas, A is the number of electrons required to generate one H$_2$ or O$_2$ molecule (two for H$_2$, four for O$_2$) and F is the Faraday constant (96485.33 C mol^{-1}).

7. Electrochemical measurements

Electrolysis experiments were performed in a standard three-electrode cell, which was composed of working electrode (Fe$_2$O$_3$-based photoanodes), counter electrode (Pt foil) and reference electrode (Ag/AgCl, sat. KCl). 1 M KOH was used as the electrolyte. The OER properties were performed from 0.2 to 2.0 V vs. Ag/AgCl with a scan rate of 5 mV s^{-1}. Electrochemical active surface areas (ECSA) were measured by cyclic voltammetry (CV) at the potential window -0.45 ~ -0.35 V vs. Ag/AgCl, with different scan rates of 10, 30, 50, 70, 90 and 110 mV s^{-1}. By plotting the $\triangle J = (J_a - J_c)$ at -0.4 V vs. Ag/AgCl against the scan rate, the linear slope which is twice of the double-layer capacitance (C_{dl}) is used to represent ECSA.

8. DFT calculation methods

The calculations in this study were performed using the CASTEP software based on density functional theory (DFT). The generalized gradient approximation (GGA) of Perdew-Burke-Ernzerh (PBE) and OTFG ultrasoft pseudopotential were chosen for the exchange-correlation function. Geometry optimization was performed until the maximum atomic energy, atomic forces and displacement were converged to 10^{-5} eV, 0.03 eV•Å^{-1} and 0.001 Å by the Broyden-Fletcher-Goldfarb-Shanno (BFGS) method.

The self-consistent-field (SCF) tolerance was set at 10^{-6} eV. To construct the FeOOH/Fe$_2$O$_3$ heterojunction, three-layer p (2×2) Fe$_2$O$_3$ (110) and single layer of FeOOH molecules periodic slabs were built with a 20 Å vacuum layer. A 2×3×1 k-point mesh was applied for the heterojunction cell with a cutoff energy of 600 eV. The Hubbard U correction was employed to account for the strong onsite Coulombic repulsion. We adopted the effective Hubbard U values of 4.3 eV for Fe 3d orbitals.

During the geometry optimization, all atoms could relax except for the bottom layer of Fe_2O_3. To construct a heterojunction model containing oxygen vacancy, two oxygen atoms on the diagonal of the surface of iron oxide were removed for introducing oxygen vacancy, and then the FeOOH molecule was adsorbed.

Supplemental Figures
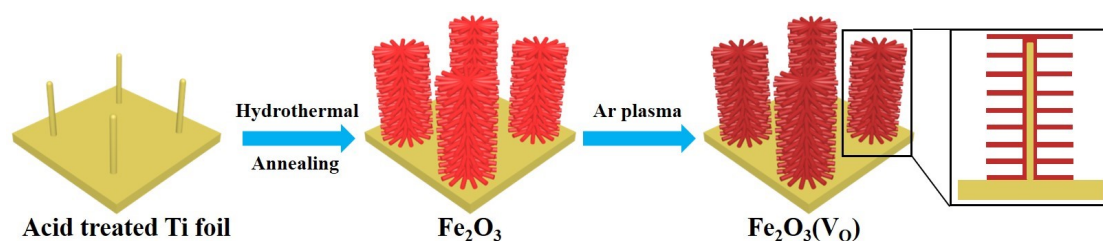
Scheme S1. Schematic illustration of the fabrication routes in this work.

Additional discussion

Firstly, the acid treatment of Ti foils was performed in a concentrated hydrochloric acid at 80 °C for 30 min. Then, FeOOH nanorods were in-situ grown on the acid-treated Ti foils via a hydrothermal process, and transformed into Fe_2O_3 after annealed at 550 °C for 2h.
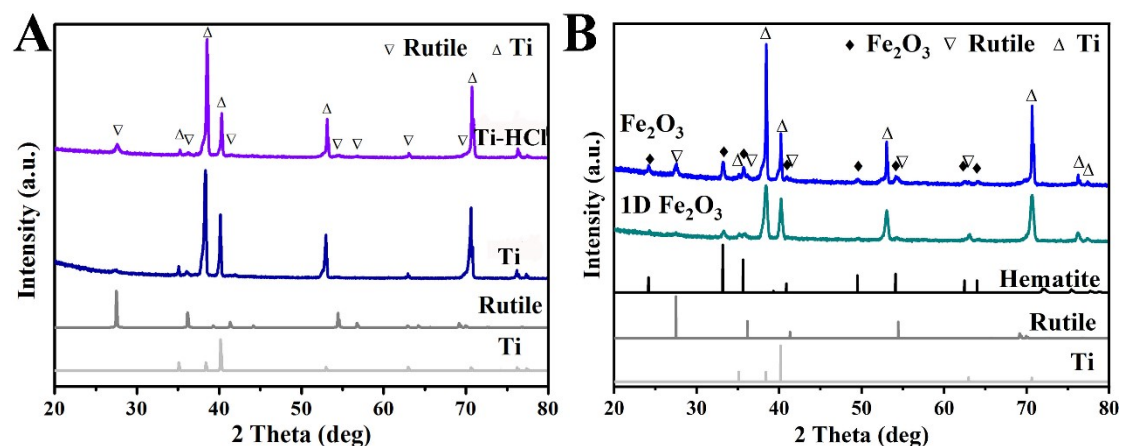
Figure S1. (A) XRD patterns of Ti foils with/without acid-treated and annealed at 550 °C. (B) XRD patterns of 1D Fe_2O_3 and Fe_2O_3.
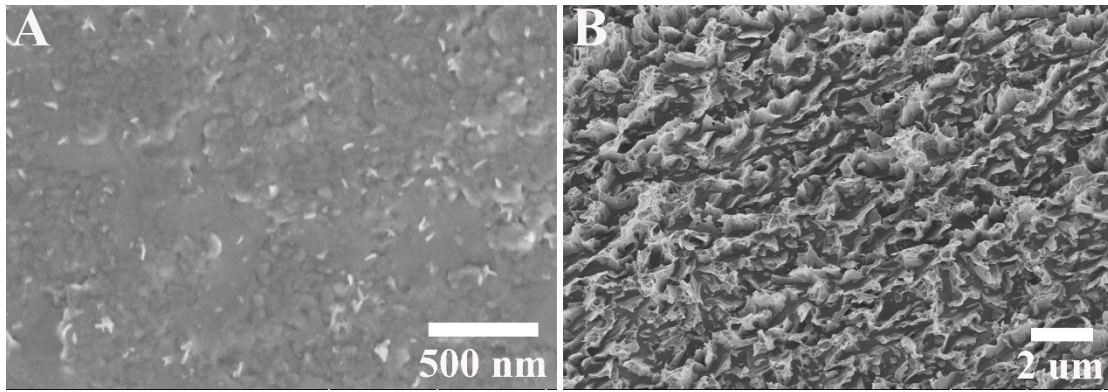
Figure S2. SEM images of Ti foils without (A)/with (B) HCl treatment at 80 °C for 30 min.

Additional discussion

As shown in Figure S2, the flat surface of Ti foils become wrinkled after acid treatment, which may be the root cause for the formation of 3D dendritic structure.
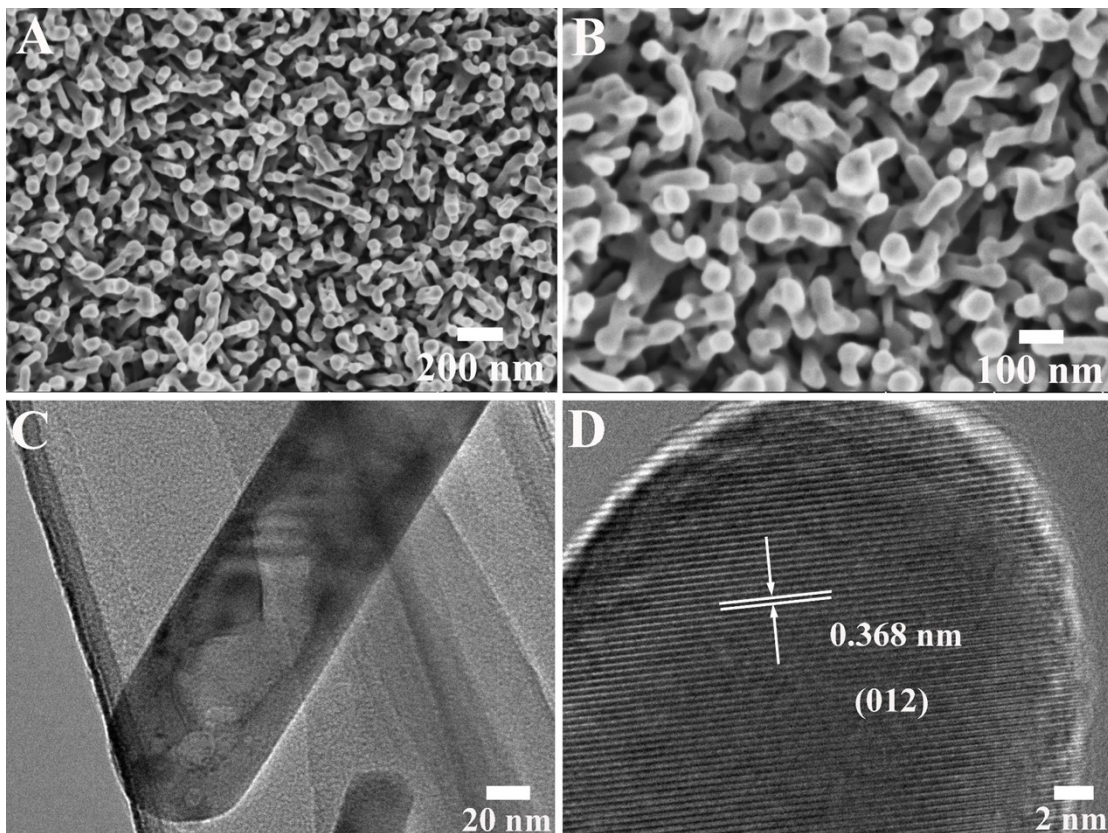
Figure S3. (A, B) SEM, (C) TEM and (D) HRTEM images of 1D Fe_2O_3.

Additional discussion

Under the same condition, 1D Fe_2O_3 nanorod arrays vertically grown on Ti foils without the acid treatment. The diameter of Fe_2O_3 nanorod are approximately 60 nm, and the high-resolution transmission electron microscopy (HRTEM) image shows an orderly lattice spacing of 0.368 nm, which correspond to the (012) crystal plane of α-Fe_2O_3.
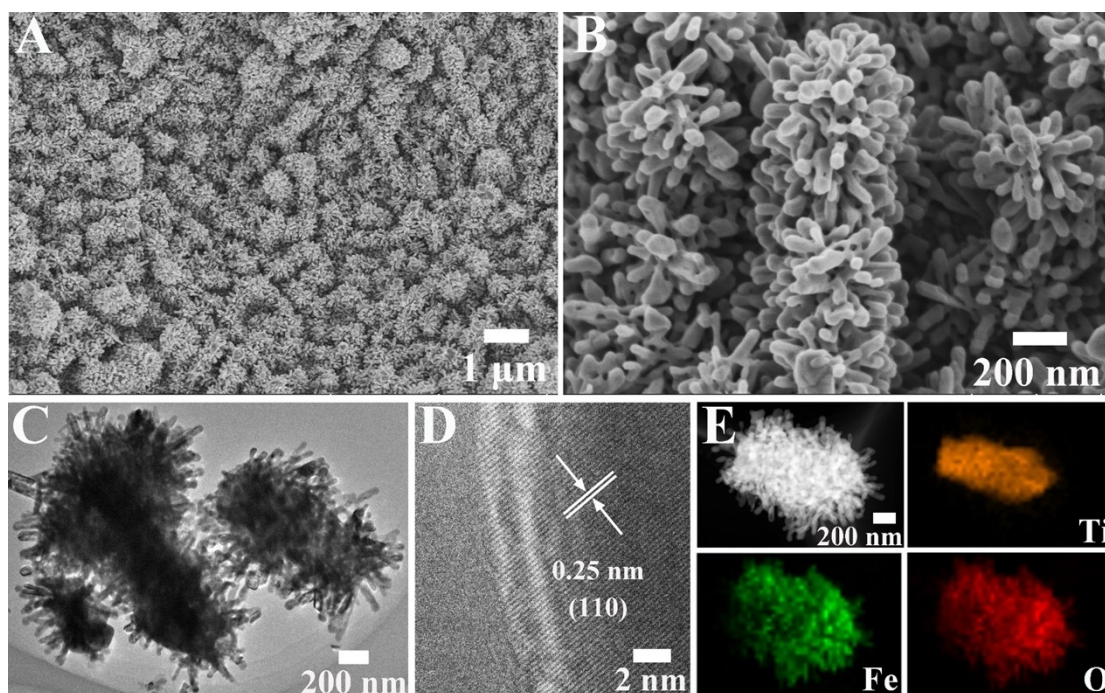
Figure S4. (A, B) SEM, (C) TEM and (D) HRTEM images of Fe_2O_3. (E) Bright-field image of Fe_2O_3 and corresponding EDS elemental mapping for Ti, Fe, O, respectively.

Additional discussion

Energy-dispersive spectroscopy (EDS) elemental mapping shows that Ti element is also detected except Fe, O elements and mainly distributed in the central region of an individual 3D dendritic structure.
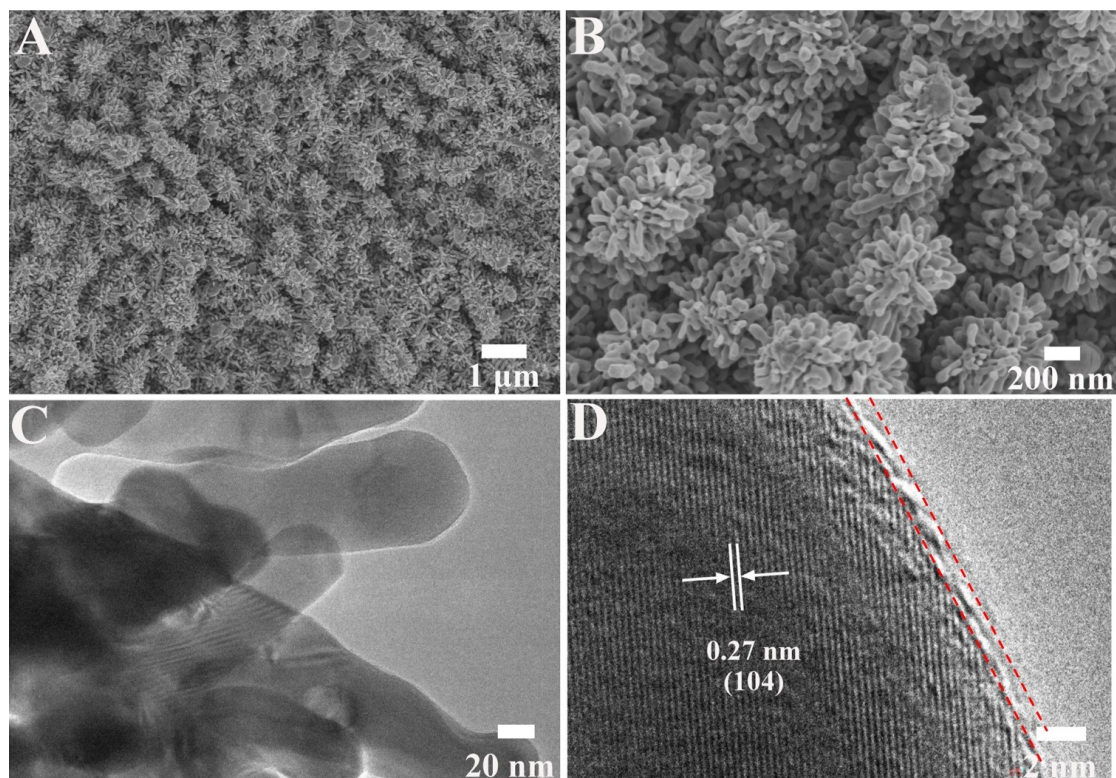
Figure S5. (A, B) SEM, (C) TEM and (D) HRTEM images of $Fe_2O_3(V_O)$.

Additional discussion

Figure S5A and B show SEM images of Fe_2O_3 treated by Ar-plasma ($Fe_2O_3(V_O)$), there is no apparent change compared with the pristine Fe_2O_3 samples. the high-resolution transmission electron microscopy (HRTEM) image shows an orderly lattice spacing of 0.27 nm, which correspond to the (104) crystal plane of α-Fe_2O_3. However, an ultrathin disordered layer with the thickness of 1 nm has been uniformly formed on the outer surface of Fe_2O_3 nanocrystals (Figure S5D), which should be resulted from the formation of surface defect sites during Ar-plasma engraving.
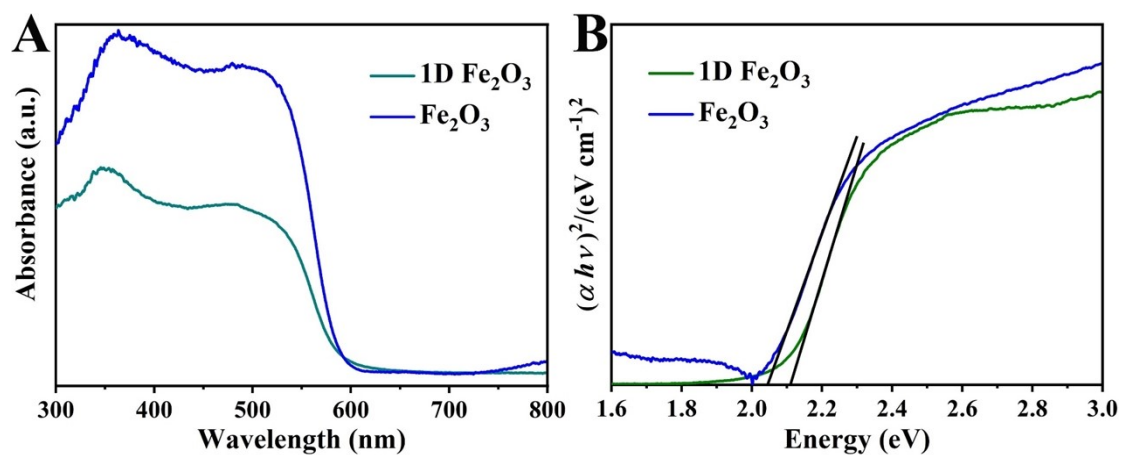
Figure S6. (A) UV-Vis absorption spectrum and (B) Tauc plot of 1D Fe_2O_3 and Fe_2O_3 photoanodes.
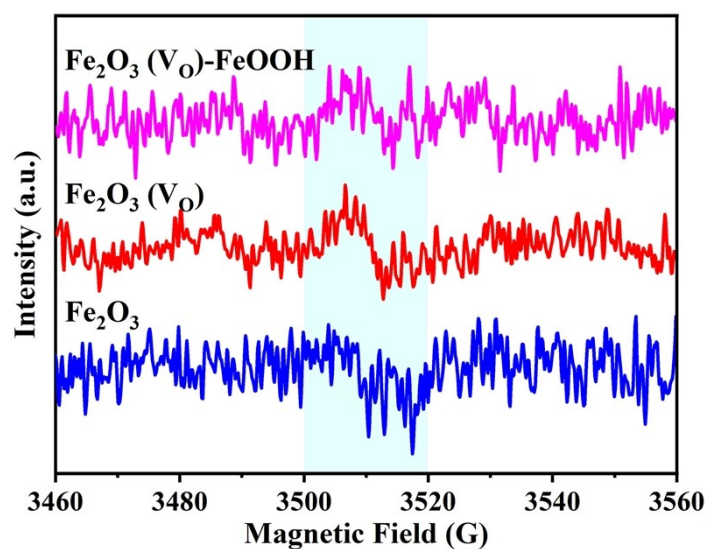
Figure S7. EPR spectra of Fe_2O_3, Fe_2O_3 (V_O) and Fe_2O_3 (V_O)-FeOOH photoanodes.

Additional discussion

The oxygen vacancy is further confirmed by low-temperature electron paramagnetic resonance (EPR) spectra. Generally, the content of oxygen vacancy is directly proportional to the intensity of electron paramagnetic resonance diffraction peak (Figure S7), further proving that Ar plasma-engraving induces more oxygen vacancies, in agreement with the XPS results (Figure 2D).
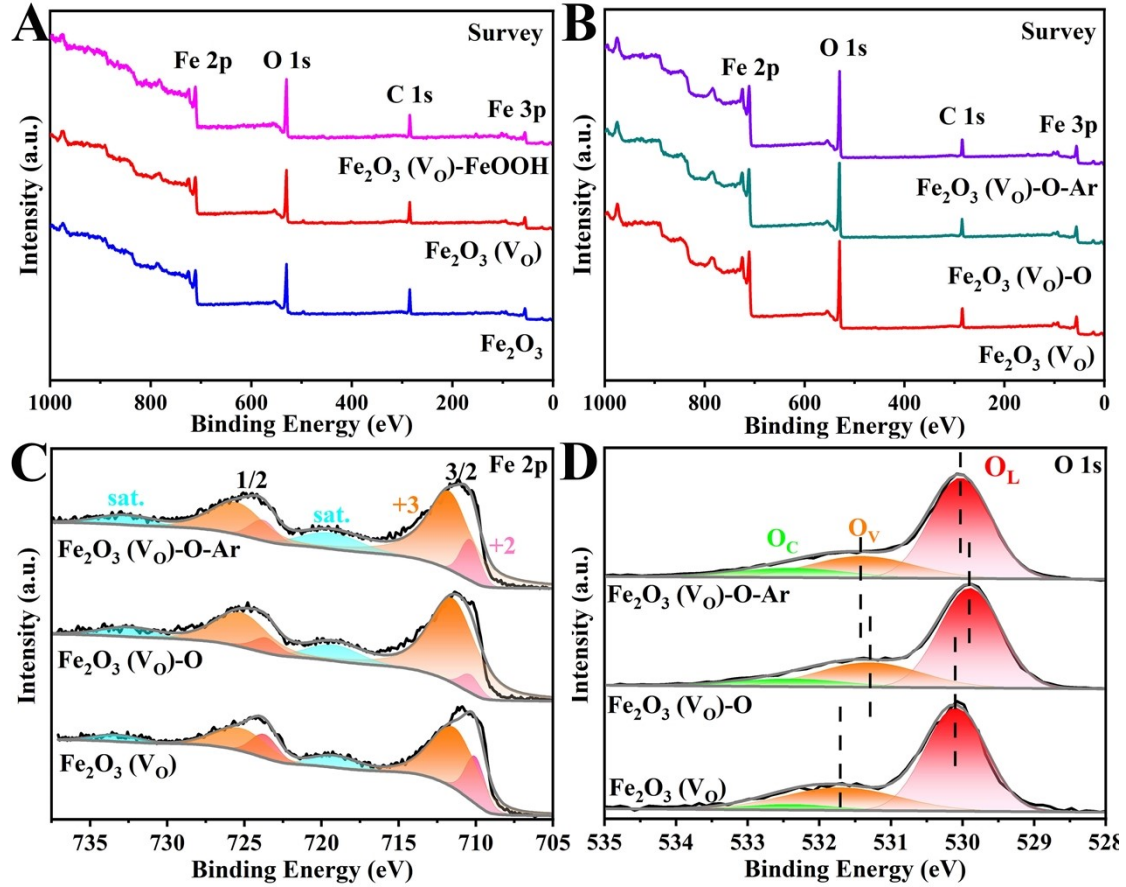
Figure S8. XPS spectra of survey, Fe 2p and O 1s for Fe_2O_3 based photoanodes.
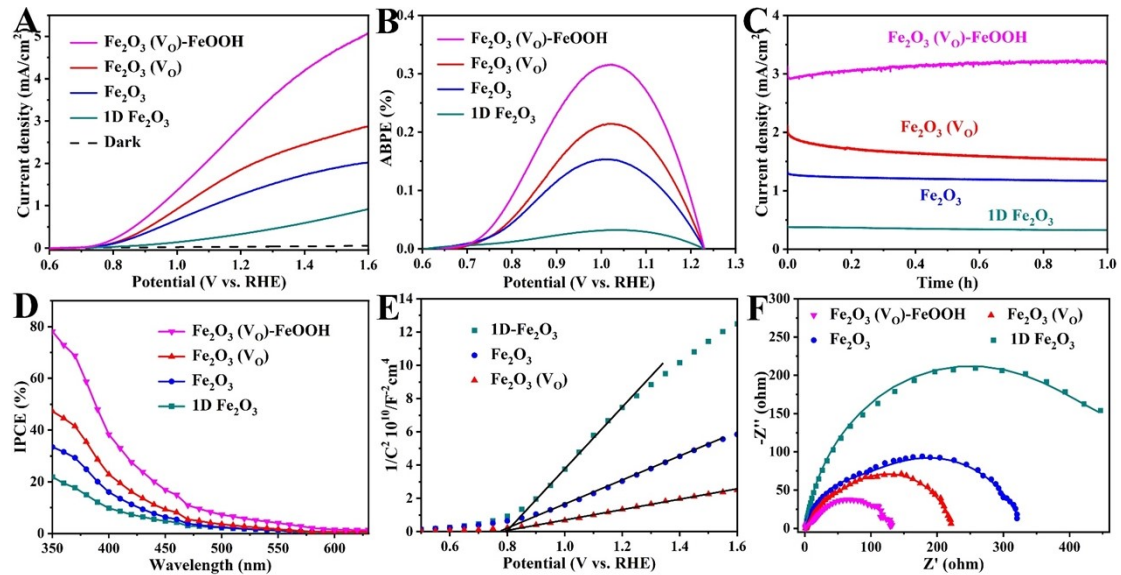
Figure S9. (A) LSV, (B) ABPE, (C) current–time curves, (D) IPCE, (E) Mott-Schottky plot and (F) EIS curves of 1D-Fe_2O_3, Fe_2O_3, $Fe_2O_3(V_O)$ and $Fe_2O_3(V_O)$-FeOOH photoanodes. All the measurements were carried in 1 M KOH electrolyte.

Additional discussion

The photoelectric conversion capabilities of samples were also evaluated by incident photon-to-current conversion efficiency (IPCE, Figure S9D). As for the IPCE results, the value of $Fe_2O_3(V_O)$-FeOOH photoanode is around 79 % at 350 nm, which is nearly four times higher than that of 1D Fe_2O_3 photoanode. From the Mott-Schottky plot shown in Figure S9E, the carrier density of 1D Fe_2O_3, Fe_2O_3 and $Fe_2O_3(V_O)$ were investigated. The smaller slope of $Fe_2O_3(V_O)$ indicates that 3D dendritic structure and the oxygen vacancies can enhance the carrier concentration of Fe_2O_3 crystals, which can result in effective charge migration and suppress bulk recombination.
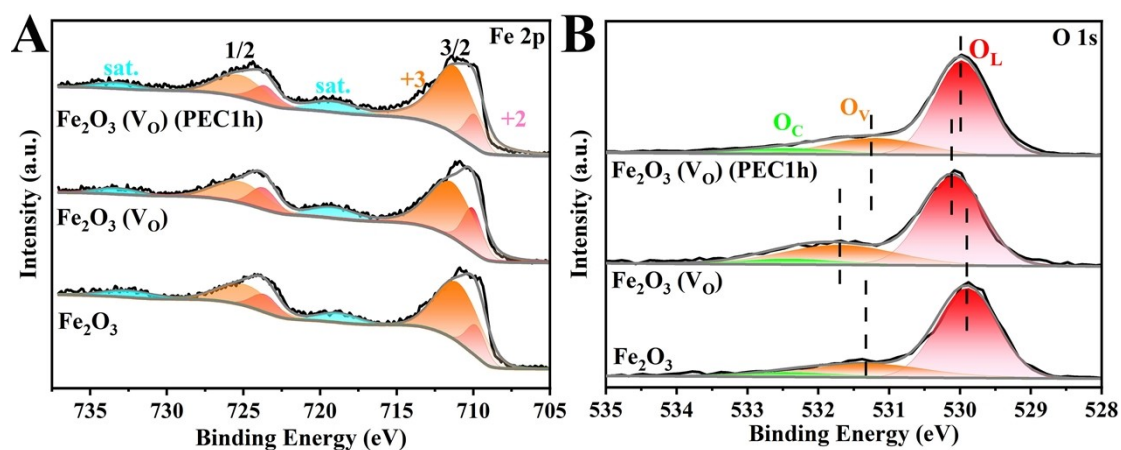
Figure S10. (A) Fe 2p and (B) O 1s XPS spectra of Fe_2O_3, $Fe_2O_3 (V_O)$ and $Fe_2O_3(V_O)$ (PEC1h).
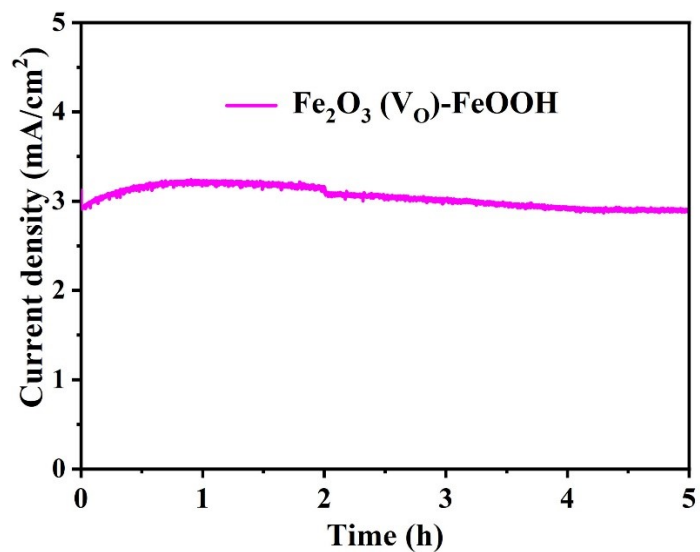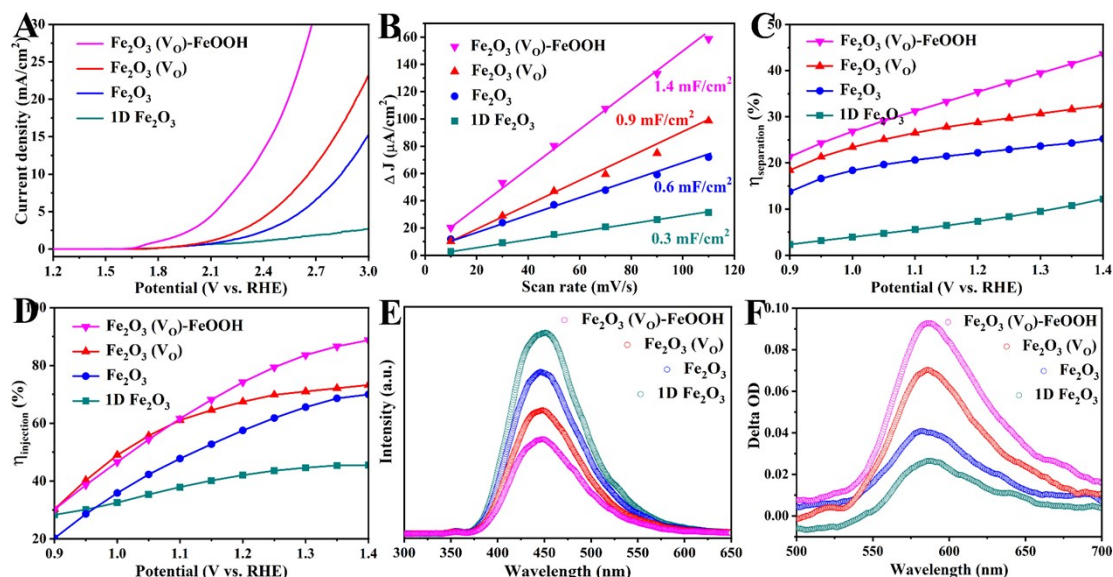
Figure S11. The long-term stability of $Fe_2O_3(V_O)$-FeOOH photoanode was conducted in 1 M KOH at 1.23 V_{RHE} under AM 1.5G illumination.
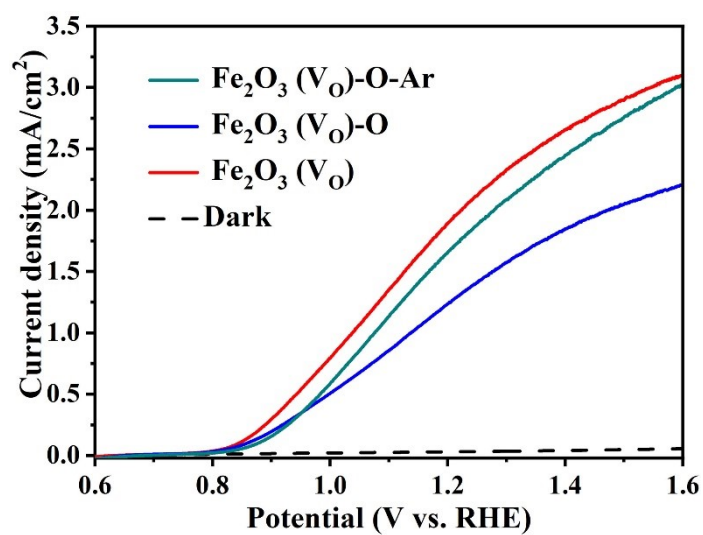
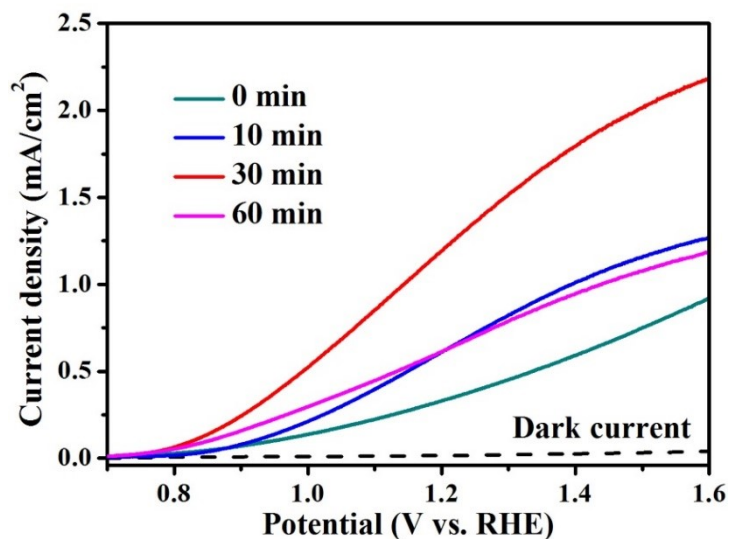**Figure S12.** LSV curves of $Fe_2O_3(V_O)$, $Fe_2O_3(V_O)$-O and $Fe_2O_3(V_O)$-O-Ar photoanodes.
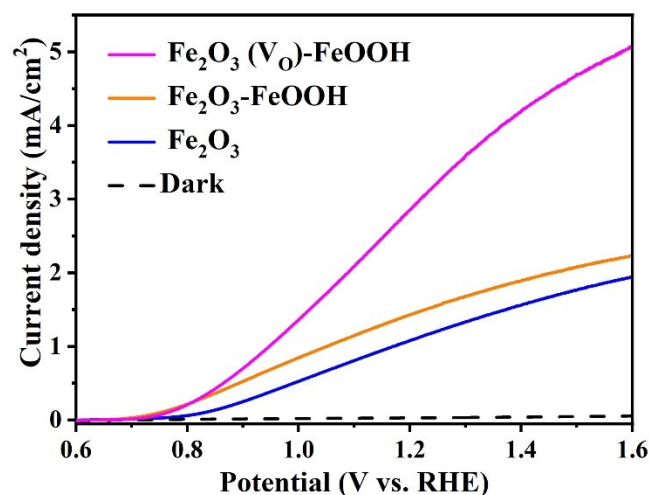
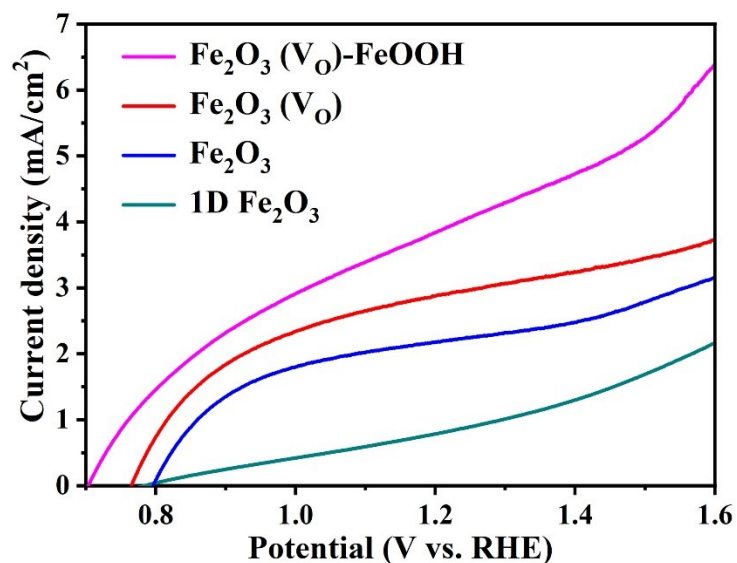**Figure S13.** LSV curves of Fe_2O_3, Fe_2O_3-FeOOH and $Fe_2O_3(V_O)$-FeOOH photoanodes.

Figure S14. (A) The OER performances were measured at scan rate of 5 mV/s. (B) Charging current density differences plotted against scan rates. The linear slope, equivalent to twice the double-layer capacitance (C_{dl}), was used to represent the ECSA. (C) Charge separation efficiencies ($\eta_{separation}$) and (D) charge injection efficiencies ($\eta_{injection}$). (E) Photoluminescence spectra excited with 355 nm light from a pulsed laser. (F) Transient absorption spectra collected at a delay time of 1 μs after excitation (λ_{exc} 355 nm).
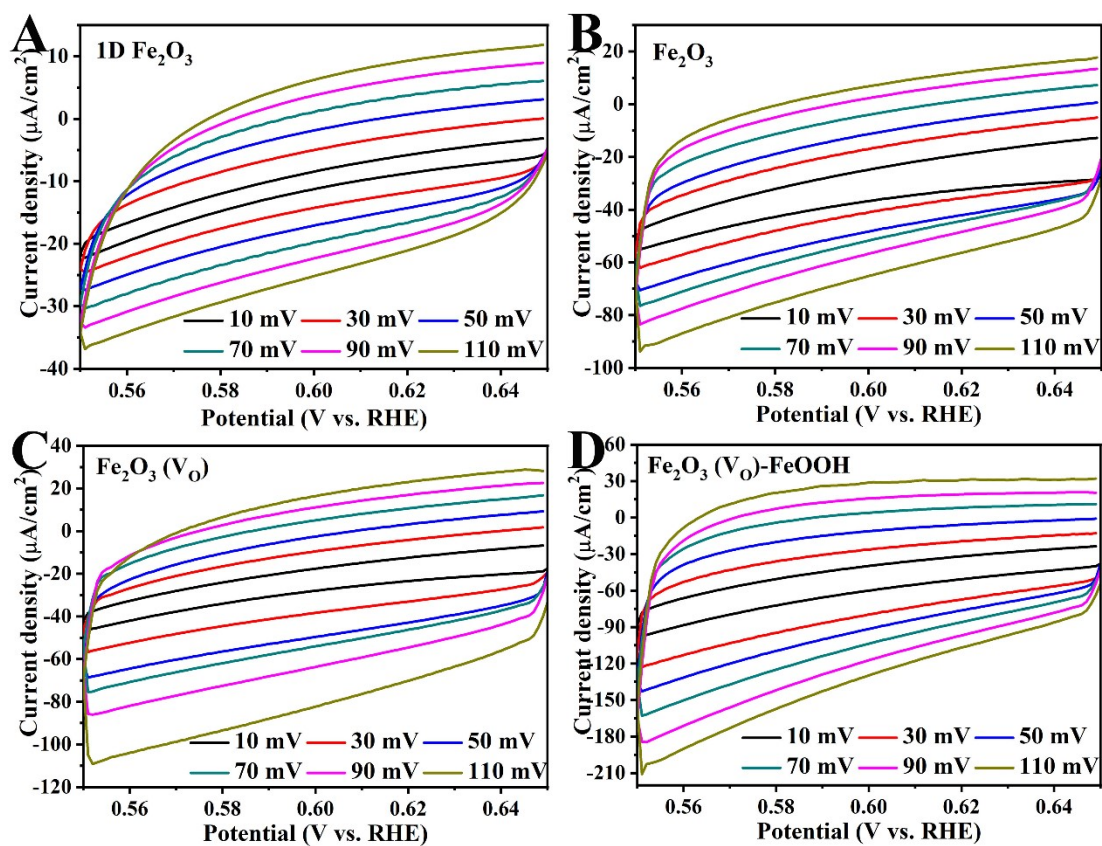
Figure S15. LSV curves of Fe_2O_3 photoanodes based on the different treatment time by HCl for Ti foils.
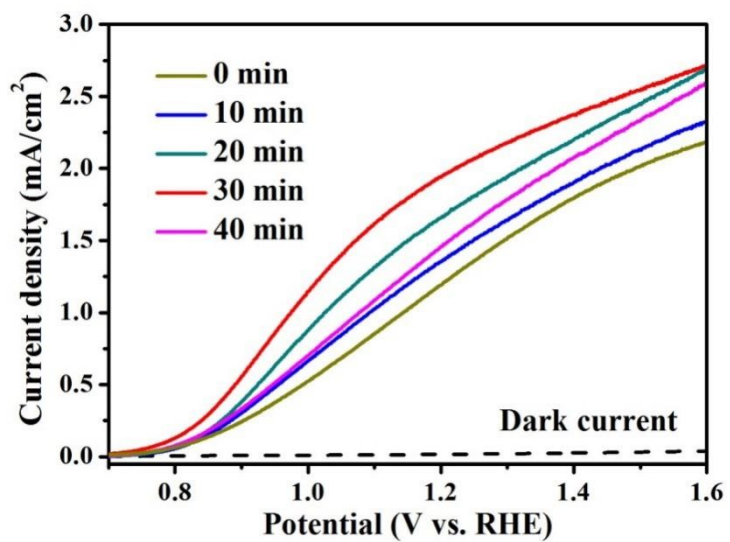
Figure S16. LSV curves of Fe_2O_3 photoanodes with Ar plasma treatment with the different time.
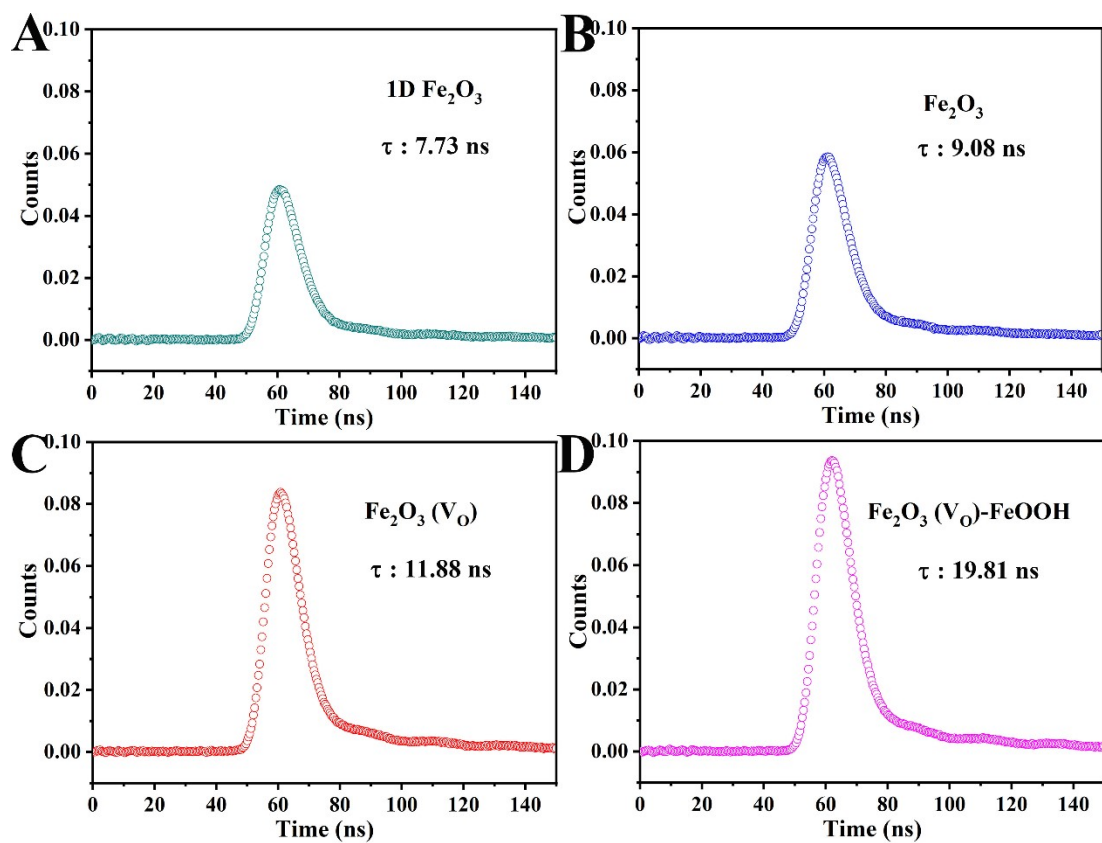
**Figure S17.** LSV curves of 1D Fe_2O_3, Fe_2O_3, $Fe_2O_3(V_O)$ and $Fe_2O_3(V_O)$-FeOOH photoanodes for H_2O_2 oxidation.

Figure S18. Electrochemical surface area (ESCA) tests towards OER in 1 M KOH. CV curves of 1D Fe_2O_3(A), Fe_2O_3(B), $Fe_2O_3(V_O)$ (C) and $Fe_2O_3(V_O)$-FeOOH (D) with different scanning rates.

Figure S19. Time-resolved photoluminescence spectra monitored at 450 nm. All samples were excited with 355 nm light from a pulsed laser.

🟣 Fe   🔴 O   🟢 V$_O$ 🩷 F$_O$ ⚪ H
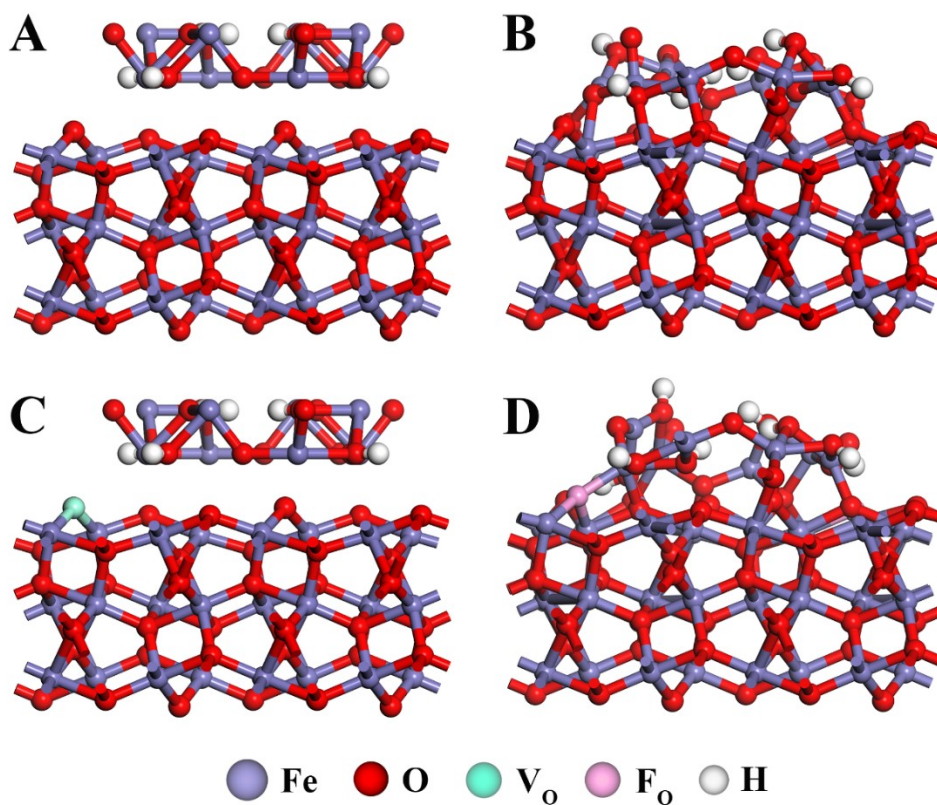
Figure S20. The theoretical atomic models of Fe$_2$O$_3$-FeOOH (A) before and (B) after geometric

optimization, Fe$_2$O$_3$(V$_O$)-FeOOH photoanodes (C) before and (D) after geometric optimization. V$_O$ represents an oxygen vacancy, and F$_O$ represents filled oxygen atoms.
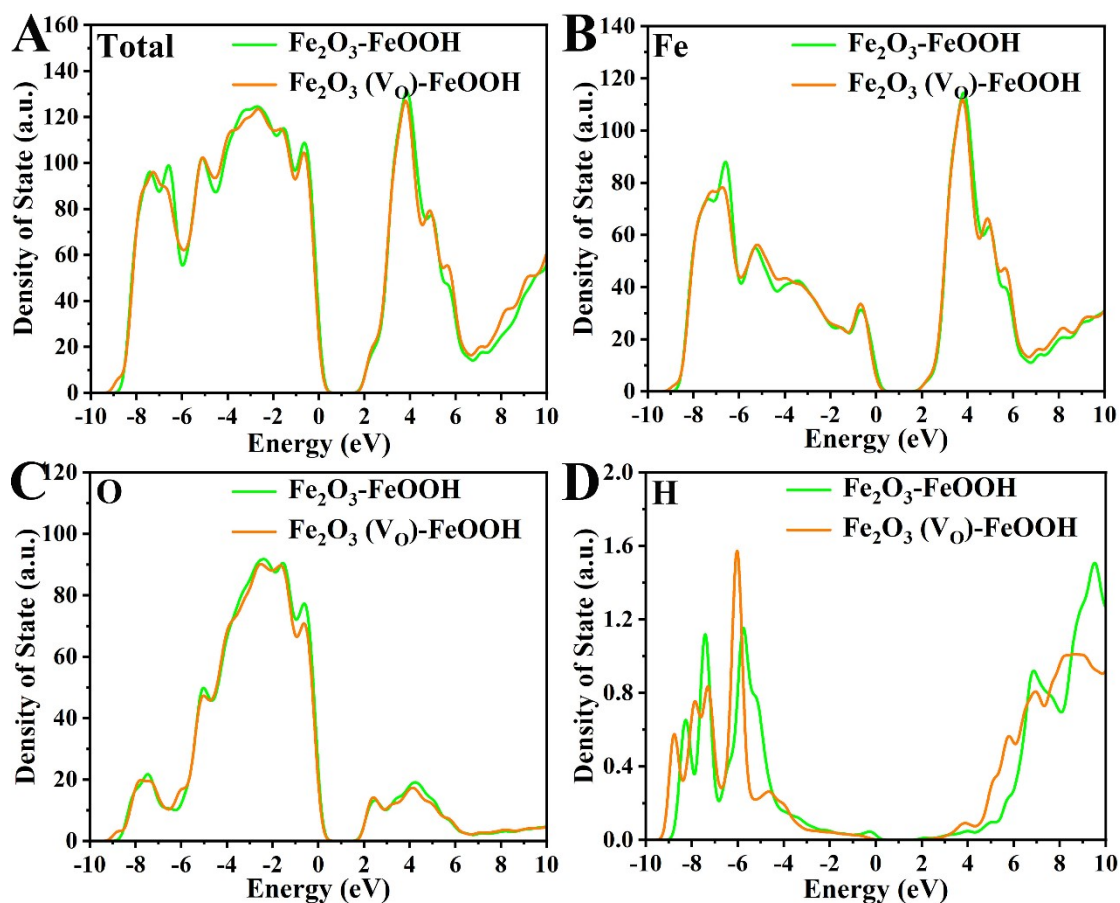
Figure S21. The total DOS (A) and PDOS (B-D) of Fe$_2$O$_3$-FeOOH and Fe$_2$O$_3$(V$_O$)-FeOOH.

Additional discussion

In Figure S21A, the total density of state (DOS) of the conduction band of the Fe$_2$O$_3$(V$_O$)-FeOOH were enhanced within the range of 5-9 eV due to the formation of the interfacial bonding, which is conducive to charge transfer. In detail, the partial density of state (PDOS) of O atoms in the Fe$_2$O$_3$(V$_O$)-FeOOH decreases, while the Fe and H atoms increases because of the interfacial bonding, this result ultimately leads to in an overall increase in the total DOS.

Table S1. The fitted results using the equivalent model for EIS measurements.

Photoanode	R_s (Ω)	R_{ct1} (Ω)	R_{ct2} (Ω)	CPE
Fe_2O_3 (V_O)-FeOOH	1.3	9.1	117.8	3.36×10^{-4}
Fe_2O_3 (V_O)	1.4	49.1	172.8	1.69×10^{-4}
Fe_2O_3	1.48	68.49	259.6	6.02×10^{-5}
1D Fe_2O_3	1.49	429.9	230.9	1.24×10^{-5}